Thin Solid Films 612 (2016) 472–482

Contents lists available at ScienceDirect

Thin Solid Films

journal homepage: www.elsevier.com/locate/tsf

Structural study of epitaxial $LiCoO_2$ films grown by pulsed laser deposition on single crystal $SrTiO_3$ substrates

Z. Li [a], S. Yasui [c], S. Takeuchi [a], A. Creuziger [a], S. Maruyama [d], A.A. Herzing [a], I. Takeuchi [b], L.A. Bendersky [a,*]

[a] Material Measurement Laboratory, National Institute of Standard & Technologies, 100 Bureau Drive, Gaithersburg, MD 20899, USA
[b] Department of Materials Science & Engineering, University of Maryland, College Park, MD 20742, USA
[c] Materials & Structures Laboratory, Tokyo, Institute of Technology, Tokyo, Japan
[d] Department of Applied Chemistry, Tohoku University, Sendai, Miyagi 980-8579, Japan

ARTICLE INFO

Article history:
Received 11 December 2015
Received in revised form 4 May 2016
Accepted 11 May 2016
Available online 24 May 2016

Keywords:
Lithium cobalt oxide
Thin films
Epitaxy
Lithium-ion battery
Li-ion battery
Pulsed laser deposition
Transmission electron microscopy

ABSTRACT

Epitaxial $LiCoO_2$ (LCO) thin films of different orientations were fabricated by pulsed laser deposition (PLD) in order to model single-crystal behavior of intercalation cathodes during electrochemical reactions. This paper demonstrates that (1) epitaxial growth of LCO on a single crystal Nb-doped $SrTiO_3$ (Nb:STO) of different orientations occurs with a single orientation relationship; (2) surface morphology of the LCO films is established by the morphology of coalescing grains during island growth mode, whereas morphology of the grains can be visualized as different cuts from a cube with low-energy $\{104\}_{R\text{-}LCO}$ surfaces; (3) the films consist of predominately trigonal R-$LiCoO_2$ phase, with a small fraction of the occasionally present cubic c-Li_xCoO_2 phase; (4) cyclic voltammetry measurements have determined rectification at interface between LCO and Nb:STO causing bias on the oxidation part of cycling, thus preventing full cycling.

1. Introduction

Thin film-based Li-ion microbatteries are of significant interest for their envisioned application in microelectromechanical systems (MEMS), smart cards, microsensors, and biochips [1–3]. In addition, thin film electrodes, especially grown as oriented single crystals, can be utilized in model electrochemical cells to study atomistic mechanisms that govern electrochemical (EC) processes in different batteries. Such thin film electrodes with predictably oriented structures and electrode/electrolyte interfaces are extremely suitable for high quality measurements, either by transmission electron microscopy (TEM) or neutron reflectivity, that can shed light on processes occurring on the atomic scale in different battery's components. Understanding growth mechanism, structural and morphological variations and deposition conditions is essential to achieve high quality epitaxial thin film electrodes that can be utilized for reliable EC and structural measurements.

$LiCoO_2$ (LCO) is one of the first intercalation cathode materials for rechargeable Li-ion batteries that have been employed in commercial Li-ion secondary batteries [4–6]; the LCO material has been studied extensively for more than two decades, thus it is a good model structure for general studies of intercalation of Li and interfacial reactions. Studies of LCO thin films were prepared by different methods: radio frequency (RF) [7–9] and direct current (DC) sputtering [10], atomic layer deposition (ALD) [11], pulsed laser deposition [12–20], spray deposition [21,22], sol–gel coating [23,24], and chemical vapor deposition [25]. Most of the studied films were deposited on conductive metal substrates, such as stainless steel, Al, Pt, and EC measurements of the films on such substrates were straightforward; accordingly the films had polycrystalline structures.

Pulsed laser deposition (PLD) is a proven deposition method widely used for making oxide films, and typically good correspondence between target's and film's compositions is achieved. For PLD of Li-containing oxides in the oxygen pressure ranging from 5 to 200 Pa, some uncertainties in Li/Co ratio for the films are possible due to the high reactivity of Li; thus some researchers use extra Li in a target to compensate for the losses. The uncertainties in composition may result in structural and phase variations, and the structural variations in principle can affect the electrochemical properties of the LCO films [26,27]. Due to structural similarities these variations are difficult to measure by averaging X-ray diffraction (XRD), especially for the epitaxial films with strains and texture, thus TEM measurements can be revealing.

The present study is focused on structural and morphological details of epitaxial LCO films deposited by PLD on single-crystal Nb-doped $SrTiO_3$ (Nb:STO) substrates of different orientations, with emphasis on analytical and high-resolution TEM. The conductive Nb:STO substrates (resistivity $\approx 5 \times 10^{-5}\ \Omega\cdot m$) were selected for (1) inducing epitaxial growth of LCO and (2) utilization as a current collector for electrochemical

---

* Corresponding author.
E-mail address: leoben@nist.gov (L.A. Bendersky).

http://dx.doi.org/10.1016/j.tsf.2016.05.017
0040-6090/Published by Elsevier B.V.

measurements with liquid electrolytes. Research on the growth of epitaxial LCO films is rather limited, and even more limited are attempts to measure EC properties of such films. The primary objective of this work was to understand preparation of epitaxial LCO films with flat crystallographic surfaces that can be used for: (1) studying how orientation of the LCO cathode/electrolyte interface affects the EC performance; (2) studying atomic-scale processes occurring on and under the interface; and (3) utilizing the oriented LCO cathodes for growing solid electrolytes for the modeling different all-solid batteries.

Bearing in mind the possibility of Li losses, compositional variations and formation of metastable phases during deposition of thin films, it is instructive to consider Li-Co-O phases within a range of compositions deviating from the target $LiCoO_2$ composition and from the pseudo-binary $LiCoO_2$—CoO_2 system. These structures have in common the presence of close-packed planes (cpp) of oxygen atoms along which structural blocks consisting of Li and Co octahedra and tetrahedra are formed.

Partial Li—Co—O phase diagram and phase equilibrium were established [28,29]. The major ternary Li—Co—O phases of interest are derivatives from the binary Co—O phases. Equilibrium ternary Li—Co—O phase diagram shows only one ternary phase of the $LiCoO_2$ stoichiometry [30]. The phase was reported as having two structural polymorphs, the high-temperature (HT) (synthesized at temperatures higher than 400 °C) and low-temperature (LT) (<400 °C) according to the temperature of synthesis. The good electrochemical performance of the HT layered $R\overline{3}m$ HT-$LiCoO_2$ [31,32] accounts for its use in commercial Li-ion batteries. The HT-$LiCoO_2$ structure is formally derived from CoO by substitution of one Co layer with Li, thus reducing the cubic symmetry to trigonal and forming alternating layers with CoO_6 and LiO_6 octahedra. The structural relationship between HT-$LiCoO_2$ and binary Co—O phase is as follow: (1) gradual removal of Li, e.g., by electrochemical de-lithiation, goes along the Li-CoO_2 tie-line, until the deficient rock salt structure $\square_{1/2}Co_{1/2}O$ ($\square$ - vacancies), or CoO_2, is achieved; (2) substitution of Li with Co leads to the rock salt CoO phase.

LT-$LiCoO_2$ has cubic $Fd\overline{3}m$ space group and suggested to be based on a spinel structure [32,33]. Substitution of Co in 8a Wyckoff position (tetrahedral coordination) by Li in spinel Co_3O_4 will have $Li_{0.5}CoO_2$ stoichiometry, however for the $LiCoO_2$ stoichiometry the 8a Co should be removed and Li in 16c position placed. This pseudo-spinel structure (isomorphous to $Li_2Ti_2O_4$) has alternation of layers consisting of ordered arrangement of Li and Co edge-shared octahedra in 1/3 and 3/1 ratio, and appears to be the best fit for LT-$LiCoO_2$ [31,33]; thus the $R\overline{3}m$ HT- and pseudo-spinel LT-$LiCoO_2$ are polymorphs. Presence of this structure was claimed for PLD-grown films [34]. Transition from LT to HT form and coexistence of these phases at 400 °C to 600 °C temperature range was demonstrated recently with the help of vibrational spectroscopy [35]. In the course of HT-Li_xCoO_2 de-lithiation along the Li—CoO_2 line, formation of the C2/m monoclinic structure near $x = 0.5$ was identified; $Li_{1/2}\square_{1/2}CoO_2$ was determined as having 1:1 ordering of Li and $\square$ (vacancies) on the Li layer [36–39]. The monoclinic structure with 1:1 ordering, as well as with 1:2 and 2:1 ordering for $x = 1/3$ and 2/3, respectively, were predicted by first-principles calculations [40,41], however only the $x = 0.5$ phase was observed experimentally.

Early work on PLD of $LiCoO_2$ by Dahn's group [12,36] has shown that variations in processing conditions result in the formation of different phases: deposition at ambient temperature yields an amorphous by X-ray structure, whereas for higher temperatures of a substrate the deposition yields a rock-salt (22–250 °C), a modified spinel LT-$LiCoO_2$ (300–450 °C) and a layered trigonal R-3m HT-$LiCoO_2$ (680 °C) structures. Deposition at 500–550 °C produced a mixture of spinel and layered structures, and the similar mixture also forms by heating above 500 °C an amorphous film. A number of studies have shown that (001)-textured HT-$LiCoO_2$ will form on a variety of heated substrates, e.g. stainless steel, quartz glass, Pt. Both stoichiometric and with up to 30% Li-excess $LiCoO_2$ targets were successfully used to deposit the aforementioned phases [14–17,42–44]. A few works were on growth of $LiCoO_2$ films epitaxially on a single-crystal substrate, e.g. on (0001)-Al_2O_3 and on (111), (110) and (100) $SrTiO_3$ (STO) [17,18,20]. For STO the following orientation relationship with HT-$LiCoO_2$ (LCO) were established by X-ray diffraction (XRD): $(111)_{STO}//(001)_{LCO}$; $(110)_{STO}//(110)/(108)_{LCO}$; $(100)_{STO}//(104)_{LCO}$ [17,20].

2. Experimental

The epitaxial $LiCoO_2$ films with ~200 nm thickness were deposited by pulsed laser deposition (PLD) on Nb:STO single crystal substrates (0.5 wt.% doped, Furuuchi Chem. Co. Ltd. [45]) of three surface orientations, (111), (110) and (100); throughout the paper the film will be labeled as LCO(111), LCO(110) and LCO(100), respectively. The PLD conditions were: 26 Pa oxygen, 600 °C temperature of a substrate, distance between a target and a substrate 68 mm, KrF Excimer laser (248 nm) with 10 Hz repetitions and 0.8 J/cm^2 power. Extra lithium containing $Li_{1.4}CoO_2$ target from Toshima Co. was used for the depositions.

The films' phases and orientations were evaluated by a 4-axes Bruker D8 Discover* X-ray diffraction (XRD) instrument. Electron diffraction (ED) patterns were acquired from a selected area of 150 nm in diameter covering the LCO films and the STO substrate using Philips CM30 TEM at 200 kV. Cross-sectional studies of the films using FEI Titan 80–300 microscope operated at 300 kV were performed from thin lamellas prepared by focus ion beam (FIB) techniques using an FEI Nova 600 NanoLab. High angle annular dark field (HAADF)-STEM images were acquired from the prepared lamellas using a spherical aberration corrected FEI Titan 80–300 microscope operated at 300 kV. HAADF images were collected using a probe convergence angle of 24 mrad and HAADF inner and outer collection angles of 70 and 400 mrad, respectively.

Electrochemical measurement was carried out with three-electrode cells. Working electrode was LCO films deposited on conductive Nb:STO. Backside of Nb-STO was coated with Ti (20 nm)/Al (100 nm)/Au (50 nm); Al/Au layer was used in order to get ohmic contact with stainless steel current collector. Lithium metal foil was used as counter and reference electrodes. Electrolyte was 1 mol dm^{-3} $LiClO_4$/propylene carbonate (PC) from BASF (battery grade, water content <20 ppm). Cyclic voltammetry (CV) was carried out with sweep rate 0.1 mV sec^{-1}, between open circuit voltage (OCV) to 4.2 V (vs. Li/Li$^+$). Electrochemical measurement was carried out in a Ar filled glove box at 30 °C.

3. Results

3.1. Orientation relationship between LCO films and STO substrates

Representative XRD scans for STO substrates of three orientations are shown in Fig. 1a. The strongest sharp peaks are from the substrates; the remaining peaks are indexed as of the HT-LCO (R-3m, hexagonal lattice Miller indexing). For LCO(111) a family of 00*l* peaks is observed. For LCO(100) a single pronounced 104 peak is observed. For LCO(110) a pair of small peaks are seen, and the peaks are indexed as 018 and 110. The peaks can also be indexed as the cubic LT-LCO (Fm-3m, cubic lattice indexing), however the pair of peaks for LCO(110) suggests that the structure is predominately trigonal HT-LCO, which is also supported by TEM results presented below. The similarity of the cubic (C) and trigonal (R) structures can be seen in the overlap of poles of plane with similar d-spacing, as demonstrated with stereographic projections in Fig. 1b. Thus the $\{104\}_R$ planes are equivalent to $\{100\}_C$, and $\{018\}_R + \{110\}_R$ — to $\{110\}_C$. This similarity is the consequence of the oxygen anions framework with ABC-packing common for both structures; thus orientation relationship is unique for all three substrates.

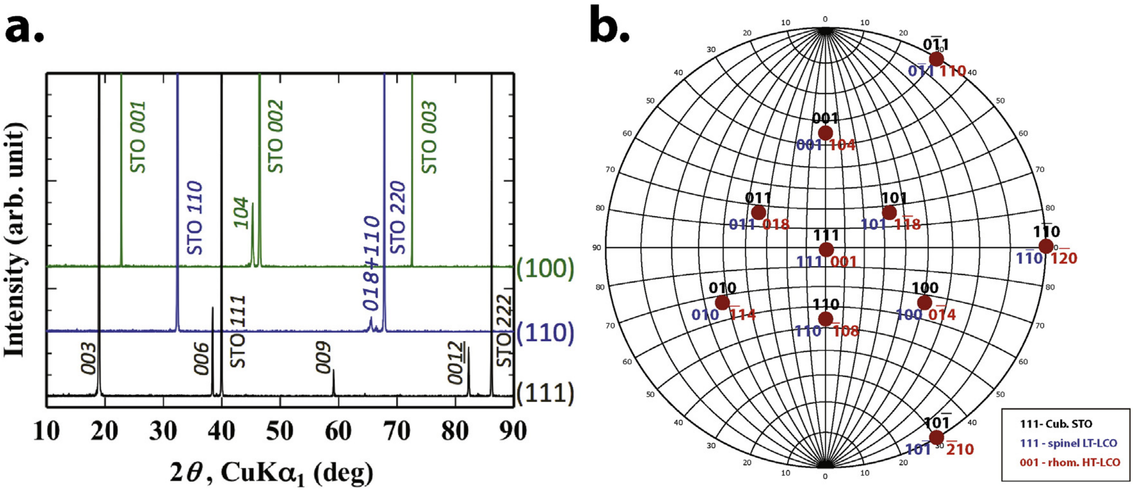

Fig. 1. (a) Out-of-plane XRD of the LCO films deposited on STO substrates in three orientations, (111), (110) and (100). The films' peaks are assigned to the trigonal HT-$LiCoO_2$; limited number of the peaks suggests that the films are epitaxial, with orientation relationship to the substrates (001)LCO//(111)STO, (110)LCO//(110)STO, and (104)LCO//(001)STO. (b) Stereographic projections of STO, R-LCO and C-LCO according to orientation relationships from XRD showing orientation relationship unique for all three substrates.

The XRD scans in Fig. 1a look very similar to those published for different $LiTMO_2$ (TM = Co,Mn,Ni) films deposited on STO substrates of similar orientations, e.g., $LiCoO_2$ [17], $LiNi_{0.8}Co_{0.2}O_2$ [19] and $LiNi_{0.5}Mn_{0.5}O_2$ [46]. These $LiTMO_2$ films were indexed as having the same trigonal phase, and XRD utilizing both the out-of-plane and in-plane techniques determined the following orientation relationships:

$$\begin{aligned}&(111)\text{STO substrate}: (111)_{STO}//(001)_{R\text{-}LTMO}, [110]_{STO}//[110]_{R\text{-}LTMO};\\&(110)\text{STO substrate}: (110)_{STO}//(110)_{R\text{-}LTMO}; [111]_{STO}//[001]_{R\text{-}LTMO};\\&(100)\text{STO substrate}: (100)_{STO}//(014)_{R\text{-}LTMO}; [011]_{STO}//[1-20]_{R\text{-}LTMO}.\end{aligned}$$

The $018_{R\text{-}LTMO}$ peak observed in our work was not considered as a possible orientation of the film on (110)STO in these publication ; as we will show below, it is in fact the most plausible orientation. For the $LiMn_2O_4$ films on (111)STO substrate in [42] the deposited phase was a cubic spinel-like structure and the orientation relationship was determined as: $(111)_{STO}//(111)_{C\text{-}LMO}$, $[011]_{STO}//[220]_{C\text{-}LMO}$; the same orientation relationship would be expected for the cubic (C) LT-LCO according to the stereographic projection in Fig. 1b.

Confirmation of orientation relationships between the films and STO came from examining selected area electron diffraction patterns (SAED) obtained from cross-sectional TEM samples. Fig. 2a shows a SAED pattern from the LCO(111) sample taken with a selected area aperture that includes both film and substrate in $[1\text{–}10]_{STO}$ zone axis orientation. The film's strong reflections are indexed as of HT-LCO in [100] zone axis (its cell is outlined with dashed lines), thus establishing the orientation relationship with STO as $(111)_{STO}//(001)_{R\text{-}LCO}$, $[110]_{STO}//[100]_{R\text{-}LCO}$. Additional weak reflections indicated with white circles and stars in the schematic drawing, Fig. 2b, are from orientational variants (twins) of R-LCO rotated either 60° or 180° around c-axis (the [110] or [−100] zone axes) and double diffractions (DD). Addition rows of very weak reflections (encircled in Fig. 2a) suggest the presence of small volume fraction of the LT-LCO (e.g, LT-LCO) at [−110] zone axis.

We can summarize the analysis of LCO(111) as following: 1. The predominant phase is the trigonal HT-LCO, with a small fraction of spinel-like LT-LCO phase presents in a mixed state; 2. Both LCO phases are in orientation relationship with the STO substrate; 3. The orientation relationship and symmetry relationship between 6 mm symmetry of (111) STO surface and trigonal LCO, and the island growth mode of the films, allow the presence of rotational (60° or 180° rotation) LCO domains, and accordingly the translational, interphase and interdomain interfaces.

Fig. 3a shows a SAED pattern from a cross-sectional TEM sample of the LCO(001) film (includes scattering from STO). The substrate is in [100] zone axis (grey spots in Fig. 3b diagram), and the LCO reflections are indexed as those of the [48-1] zone axis of R-LCO, Fig. 4b. The R-LCO

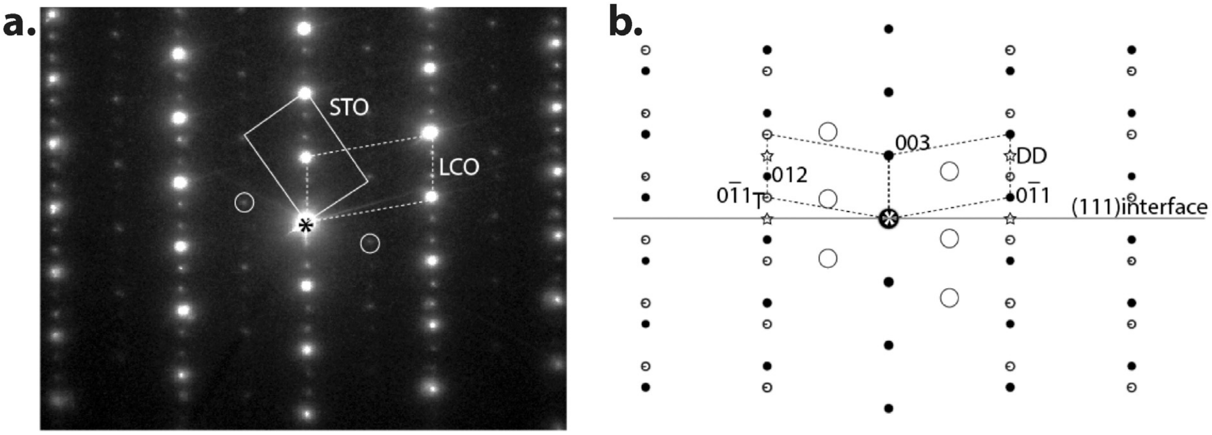

Fig. 2. (a) SAED pattern from the LCO(111) sample taken with a selected area aperture that includes both a film and a substrate in $[1\text{–}10]_{STO}$ zone axis orientation. (b) The strong reflections are indexed as of R-LCO in [100] zone axis (its cell is outlined with dashed lines), thus establishing the orientation relationship with STO as $(111)_{STO}//(001)_{R\text{-}LCO}$, $[110]_{STO}//[100]_{R\text{-}LCO}$.

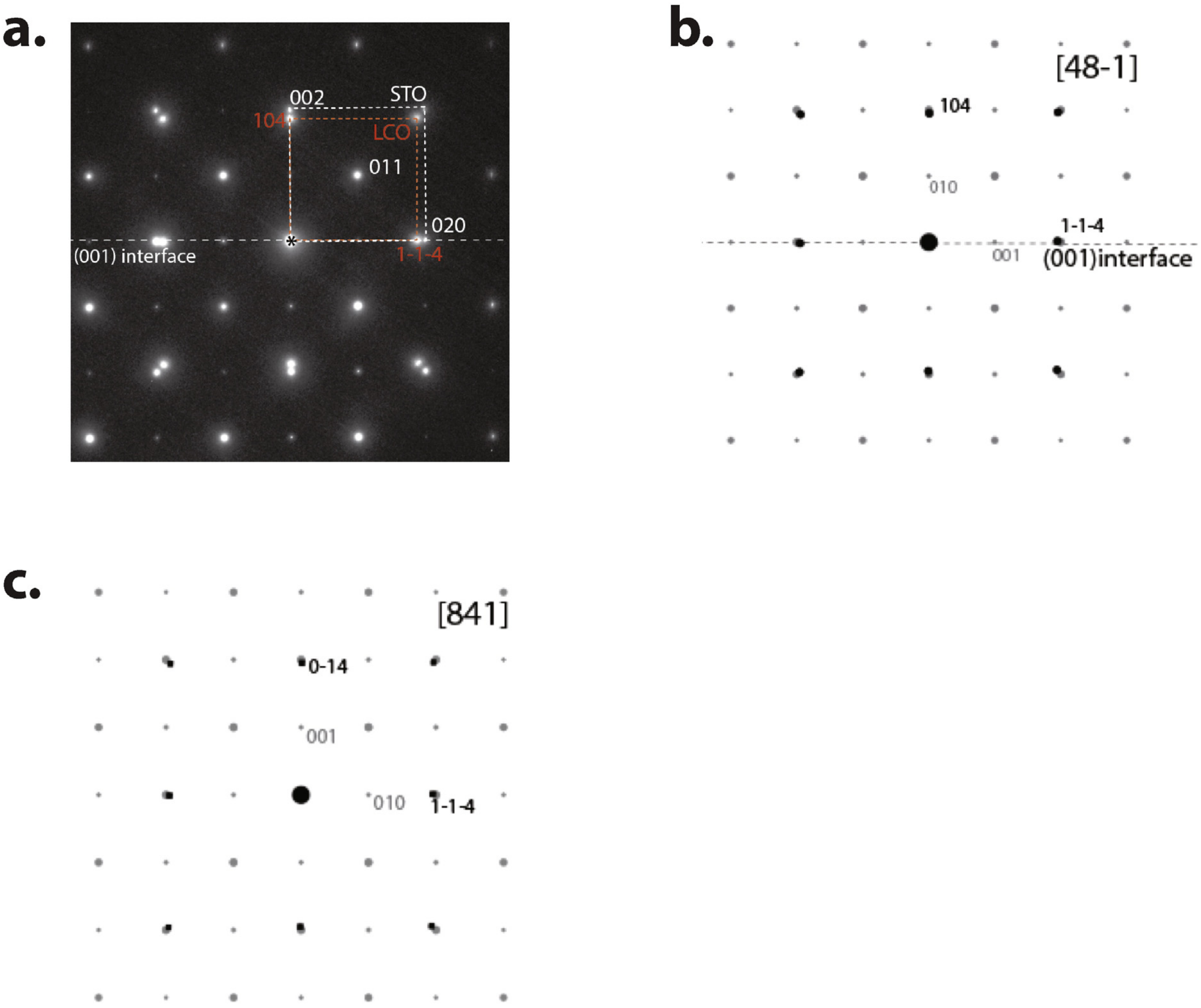

Fig. 3. (a) SAED pattern from the LCO(001) sample taken with a selected area aperture that includes both a film and a substrate in $[100]_{STO}$ zone axis orientation. (b) The substrate is in [100] zone axis (grey spots in diagram), and the LCO reflections are indexed as those of the [48-1] zone axis of R-LCO.

phase is in near perfect orientation relationship $(010)_{STO}//(01\text{-}4)_{R\text{-}LCO}$, $(001)_{STO}//(-114)_{R\text{-}LCO}$ (or $[100]_{STO}$ $//[841]_{R\text{-}LCO}$) with the STO substrate; a trace of the (100) STO surface shows that the plane parallel to the surface is (01-4) of R-LCO, which is in agreement with the XRD results. Fig. 3c shows overlapping simulated diffraction patterns for the direction normal to the substrate (010) surface (90° rotation from the patterns in Fig. 3b); the near-overlap of 0-14 and 1-1-4 LCO reflections with (002) and (020) of STO, respectively, shows structural reason for the observed epitaxy and orientation relationship. The [841] pattern has pseudo-cubic symmetry, which suggests the possibility of 90°-rotated structural variants of R-LCO, and overall six rotational variants with near identical diffractions but different directions of a unique *c*-axis.

Fig. 4a shows diffraction results for the cross-sectional TEM of the LCO(110) film; the SAED pattern is similar to the one for LCO(100) in Fig. 3a, but rotated 45° with respect to the LCO/STO interface. Diagram in Fig. 4b shows indexing of the reflections as [100] zone axis (grey circles) of STO and [841] zone axis (black circles) of R-LCO. However, due to its pseudo-cubic nature, the pattern can be rotated 90°, with either (1-20) or (10-8) parallel to the (011) plane of STO. The TEM observation is in agreement with the XRD results were peaks of both 1-20 and 10-8 were detected for this film. Overlap of simulated SAED patterns with (10-8) LCO plane parallel to (110) STO surface ([241]LCO//[110]STO) in Fig. 5c shows alignment and near-overlap of LCO and STO planes. Similarly, overlap of simulated SAED patterns with (1-20) LCO plane parallel to (110) STO surface ([100]LCO//[110]STO) shows in Fig. 5d again alignment and near-overlap of LCO and STO planes, e.g., $(104)_{R\text{-}LCO}//(001)_{STO}$, $(10\text{-}8)_{R\text{-}LCO}//(2\text{-}20)_{STO}$ and $(006)_{R\text{-}LCO}//(\text{-}1\text{-}11)_{STO}$. This compatibility of planes justifies the observed epitaxial growth on (110)STO, although SAED patterns and respective structures of (10-8) and (1-20) families contacting the (110) surface of STO are very different. It should be noted that {10-8} and (1-20} families belong to the (110) family of LCO in cubic (e.g., pseudo-spinel) representation. Considering direction of the LCO c-axis, there are six variants related by the 2 mm symmetry of the (110) surface; for (1-20)-type variants the (001) planes of easy Li-ions diffusion are normal to the film's surface, and for (10-8) – inclined about 35°. XRD of the LCO(110) film, Fig. 1a, show the preference of {108} planes, which was also observed for epitaxial LCO(110) films by Nishio et al [20].

In order to understand if the experimentally established orientation relationships for the three STO surfaces are a unique one, we've performed the following procedure. The simulated SAED patterns of both R-LCO and s-LCO were tilted/rotated the same way as the pattern of STO from the orientation relationship of the (111)-film, Fig. 5a. The set of tilt/rotations from [1-10] STO to [001] STO is shown, as well as the same set applied for [110] of R-STO and s-LCO. For the R-LCO the orientation matching [001] STO is [4-4-1] for R-LCO and [001] for s-LCO, Fig. 5c. The [4-4-1] R-LCO is matching the experimental observations, from which we conclude that there is a single crystallographic orientation relationship between the STO substrate and film, which is not depend on the orientation of a substrate.

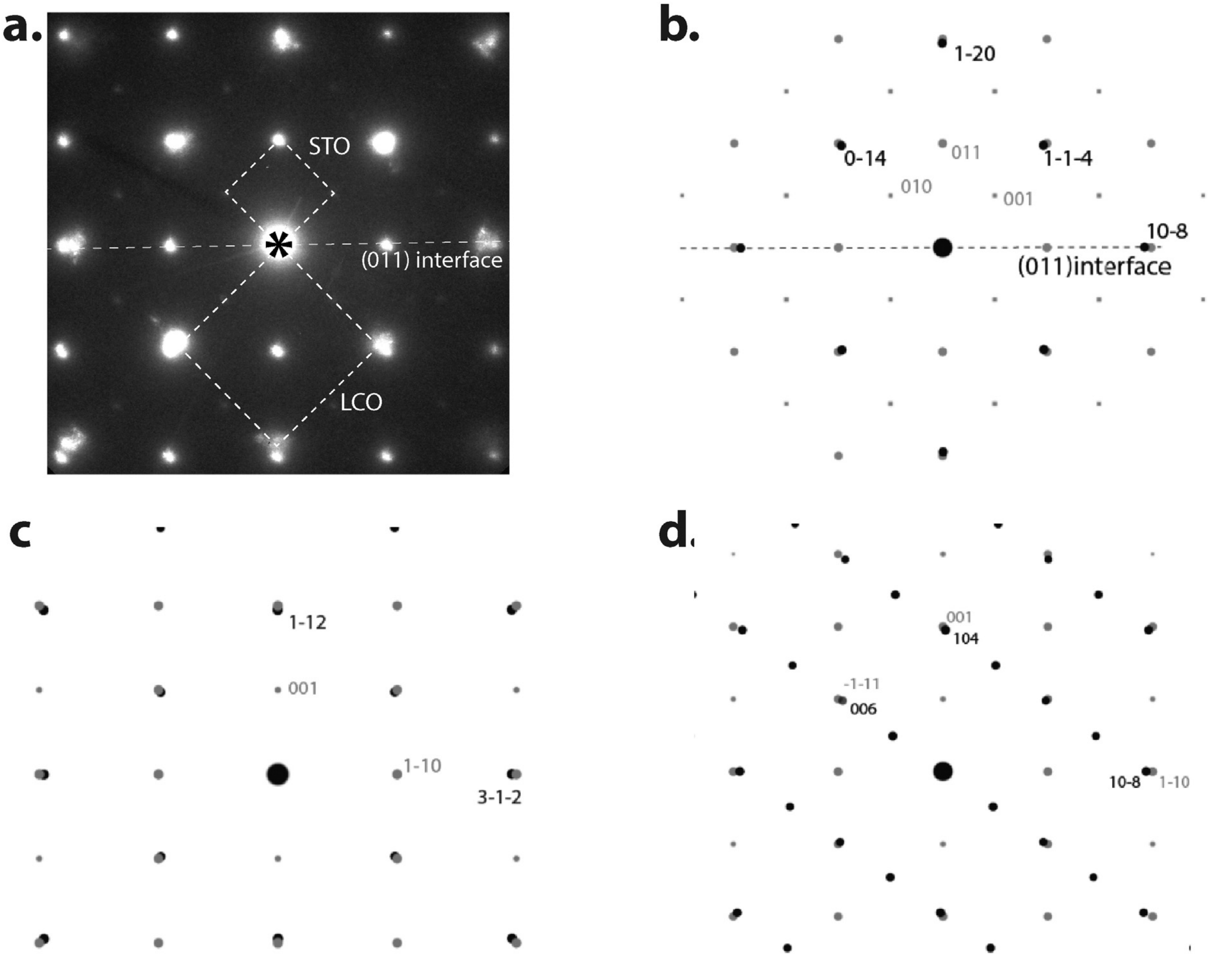

Fig. 4. (a) SAED pattern from the LCO(011) sample taken with a selected area aperture that includes both a film and a substrate in [100]STO zone axis orientation. (b) The substrate is in [100] zone axis (grey spots in diagram), and the LCO reflections are indexed as those of the [841] zone axis of R-LCO.

3.2. Morphology and growth mode of the films

Fig. 6 shows SEM images of the LCO films' surfaces. From the images it is clear that the surfaces are not flat but fragmented into domains distinguished by characteristic symmetric interfaces. Symmetries of these interfaces are in accord with the plane symmetry group of the underlying STO surfaces, namely p6mm for (111), p4mm for (100) and p2mm for (110). The domains' shape is established by the upper surface and a set of oblique surfaces. Electron Backscatter Diffraction (EBSD) measurements from individual domains were performed with the goal to identify crystallographic orientations of individual domains with respect to the observed by SEM morphological features. Examples of EBSD patterns obtained for three orientations are shown in Fig. 7; the figure shows STO poles normal to the films' surfaces.

Image from LCO(111) in Fig. 6a shows triangular domains of 3 mm symmetry covering the film's surface. Two orientations related by 180° rotation (equivalently 60°) rotation are observed with approximately equal frequency; these two orientations are subsets of the 6-fold rotation of p6mm. Occasionally similar but rotated 30° triangular domains are seen. The smallest morphological features have a shape of triangular pyramids typically residing on flat surfaces of larger domains. A surface of the film on (100)STO, Fig. 6b, shows an assembly of domain facetted to the cuboidal appearance with 4 mm symmetry. Most of the domains have more complex shapes reminding a jigsaw puzzle; these shapes apparently result from coalescence of cuboidal domains. Fig. 6c is an SEM image of a film's surface on (110)STO; the surface reminds a view of rooftops in a densely populated town. The rooftop-like domains are tightly packed and contacting each other; the domains have approximately 2 mm symmetry. Overall morphologies of the films' domains are in direct correspondence with orientations and symmetries of the substrates. For (111)STO the surface has p6mm planar symmetry, to which p3m1 planar symmetry of the domains is subgroup with two rotational variants. For (100)STO the surface has p4mm planar symmetry, which coincides with four-fold symmetry of the cuboidal domains. For (110)STO the surface has p2mm planar symmetry, which is compatible with the 2-fold symmetry.

In general, in island mode growth of films, morphology of the films' surface is established by the morphology of the coalescing islands. Morphology of the islands is established by a top surface, which is parallel to the substrate/film interface and dictated by epitaxial relationship with a substrate, and by low energy surfaces. According to Tasker [47], for ionic crystals there are three types of surfaces: type I non-polar electrically neutral with stoichiometric proportion of anions and cations, type II polar charged with no dipole moment, and type III polar with a dipole moment. Kramer and Ceder [48] using First Principles calculations have evaluated energy of these surfaces for the trigonal $LiCoO_2$ structure. The lowest energies were found for the polar (001) and non-polar {1-20} and {104} surfaces for all reasonable values of the Li and O chemical potentials. The (012) surface, however, is stable only under oxidizing conditions. The equilibrium shape is sensitive to the equilibration

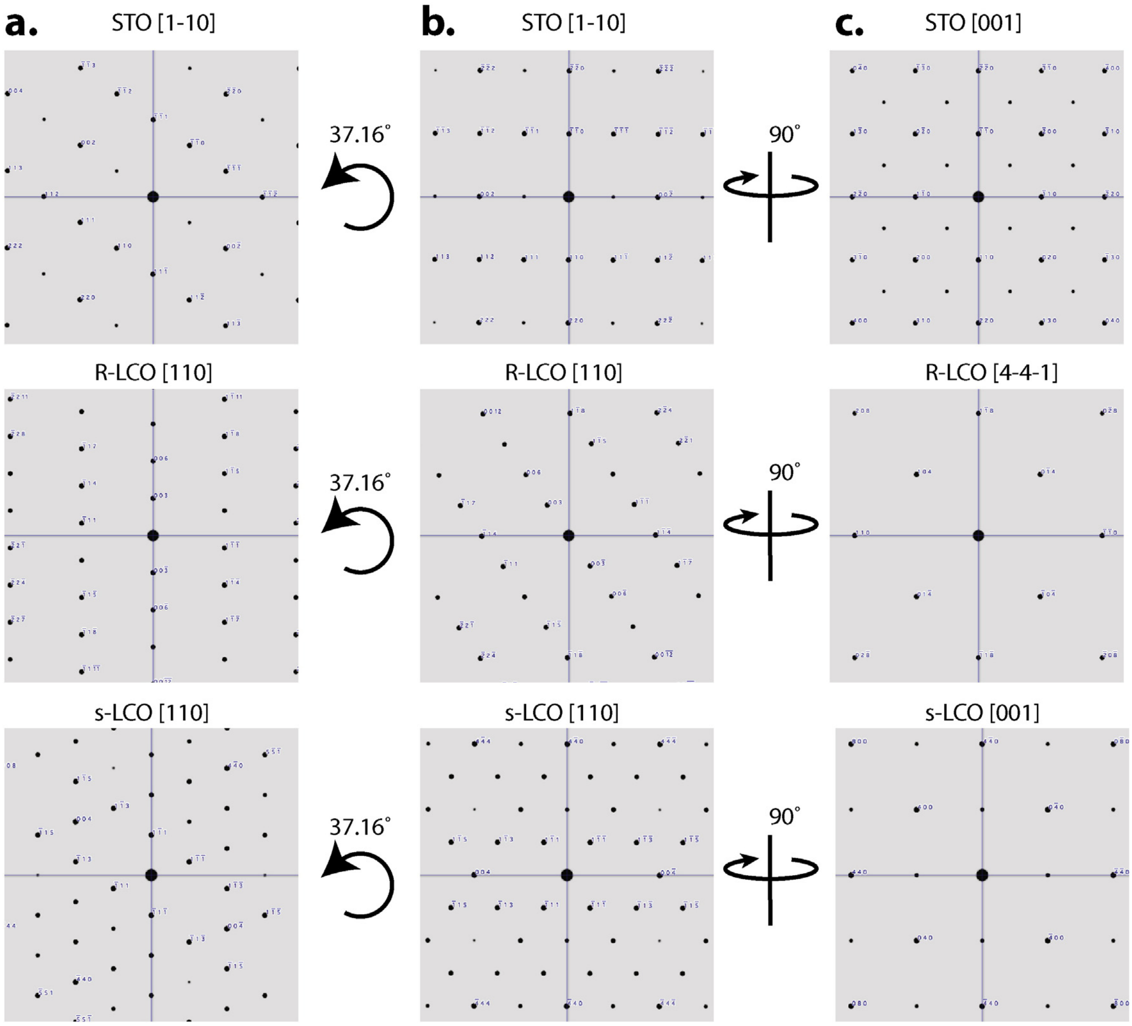

Fig. 5. (a) Simulated SAED patterns of STO, R-LCO and s-LCO in orientations established for the LCO(111) film. The patterns were tilted/rotated the same way as the STO to the orientation (b) STO [1-10] and (c) STO[001]. Scale is the same for all images.

environment because the thermodynamically favorable surface terminations and surface energies of the polar (001) and (012) surfaces are a function of environment. These theoretical predictions are in excellent agreement with our observation: (1) for LCO(111) the islands' shape of truncated triangular pyramids are formed by (001) and {104} surfaces; (2) for LCO(001) the islands' shape of cubes is formed by three {104} surfaces, and (3) for LCO(001) the islands' shape of roof-type formed by {104} when pointed, or if truncated - with an additional {1-20} surface.

3.3. TEM

3.3.1. Cross-sectional TEM samples, electron diffraction and orientation relationship

Cross-sectional TEM observations at low magnification confirm faceted roughness of the films' surfaces; e.g., a bright field image of LCO(111), Fig. 8, shows surface facets associated with individual grains/domains. The TEM image supports the film's growth mode suggested in Fig. 6; the surface facets form by impingement of the faceted grains. According to SAED patterns from the sample, all the impinging grains are oriented in accord with the established orientation relationship between LCO and the STO substrate. Cross-sectional TEM samples were also used for high-resolution TEM imaging to understand structural details of interfaces and domains, and the results for the films on all three substrates are summarized in Fig. 9.

3.3.2. Cross-sectional TEM samples: LCO/STO interfaces

Fig. 9a shows a HRTEM image of the (111)STO/LCO interface (an arrow indicates location of the interfaces). Fast Fourier Transform (FFT) patterns taken from the STO and LCO regions are shown on the right of the image. Indexing of the FFT patterns shows that the STO substrate is in $[112]_{\mathrm{STO}}$ zone axis, and the LCO film - in $[120]_{\mathrm{R\text{-}LCO}}$ of the trigonal R-LCO. However extra rows of reflections (shown encircled in the FFT) can be interpreted as either ½$110_{\mathrm{R\text{-}LCO}}$ ordering reflection of R-LCO or belonging to the s-LCO in $[112]_{\mathrm{s\text{-}LCO}}$ zone axis. These patterns support the same orientation relationship that was established in earlier analysis (in Fig. 9a the substrate/film are rotated 90° to the orientation in Fig. 2). Observation of structural details (in comparison with simulated high-resolution images) suggests that the film is predominantly the trigonal layered R-LCO structure, with some small regions showing ½$110_{\mathrm{R\text{-}LCO}}$ ordering and interpreted as having a spinel-like structure. The observed (111)STO/LCO interface appears to have a near-interface layer of one to two structural units that is structurally different from LCO, however no secondary phases or amorphous layers could be recognized at the interface. The near-interface layer is most probably the result of not atomically flat STO surface.

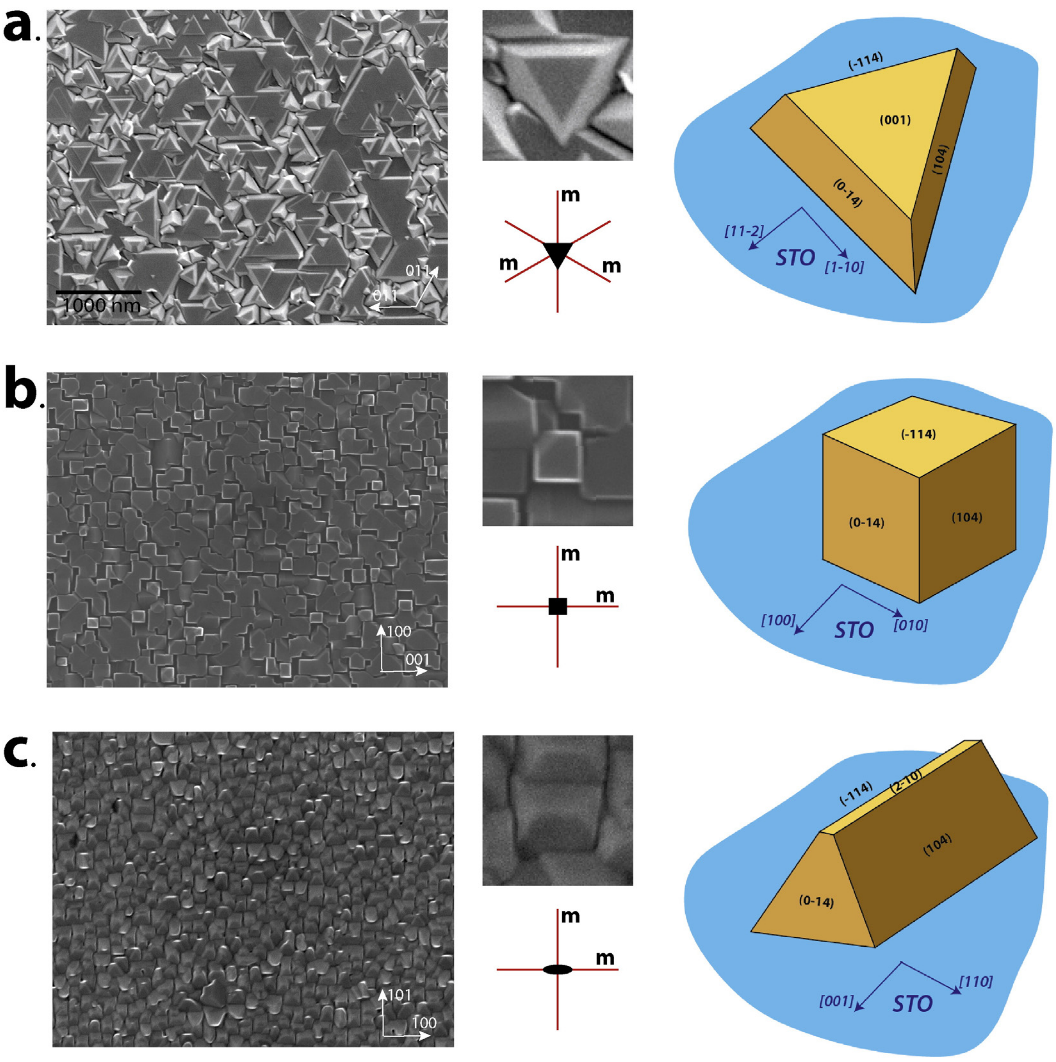

Fig. 6. SEM images of surfaces of (a) LCO(111), (b) LCO(100) and (c) LCO(110) films. Symmetry of the domains forming the films is in accord with the plane symmetry group of the underlying STO surfaces, namely (a) p6mm for (111), (b) p4mm for (100) and (c) p2mm for (110). The domains' morphology is determined by the low-energy crystallographic facets shown on the far-right side of the figure.

Fig. 9b shows a HRTEM image of the (110)STO/LCO interface. Corresponding FFT patterns on the right-hand side of the image show $[-110]_{STO}$ orientation of the STO substrate and $[100]_{R\text{-}LCO}$; for LCO the pattern also shows diffuse reflections that can be contributed by s-LCO in $[110]_{s\text{-}LCO}$ zone axis. However both the HRTEM image and FFTs suggest that the film has predominant orientation with $(018)_{R\text{-}LCO}$// $(110)_{STO}$ (also suggested in [20]), with some domains of s-LCO ($[101]_{STO}$ orientation) and 180°-rotated R-LCO (around a normal to the surface or mirror reflected). The domains and their inter-domain boundary are clearly recognized by different orientations of the $(001)_{R\text{-}LCO}$ crystallographic planes.

Fig. 9c shows a HRTEM image of a (100)STO/LCO interface; according to the FFT patterns on the right-hand side of the image, the TEM sample is in the same orientation relationship with STO as established with XRD. The observed STO/LCO interface is atomically sharp and shows direct growth of LCO on STO (100) surface without presence of foreign phases. Two variants are seen on the image

In order to gain better understanding of structural details at the STO/LCO interfaces, HAADF-STEM atomic imaging was employed. This largely incoherent imaging mode produces image contrast that is less sensitive to diffraction influences and which is often more directly interpretable than that produced in HRTEM images. Fig. 10a shows a STEM image taken from the 111-film with STO in $[110]_{STO}$ zone axis and LCO in $[110]_{r\text{-}LCO}$. The STEM image shows an atomically sharp interface where the stacking of high-Z atoms, Sr for STO and Co for LCO, on both sides of the interface is clearly seen. Enlarged part of the STEM image is shown in Fig. 10b. By overlapping the image with structural projections of corresponding STO and LCO structures (overlapping the bright spots of high-Z atoms with Sr and Co, respectively), the structural model for the interface can be analyzed, as shown in Fig. 10c. The model shows that a-b-c-stacking of oxygen ions in both SRO and LCO (outlined in the figure) is interrupted across the interface and has a-b-c-a||a-b-c sequence. Both the oxygen sequence and STEM contrast suggest that an immediate atomic layer on STO will have a mixing of Ti and Co transition metals, respectively from STO and LCO.

3.3.3. Cross-sectional TEM samples: structural variations

Fig. 11a shows a HAADF-STEM image of the (111)STO/LCO film in $[211]_{STO}$ orientation; in this region structural variations (labeled as Type I and II) are clearly seen from differences in the positions of bright spots (high-Z Co atomic columns). According to FFT from these structurally different regions, the variations are in agreement with those identified by electron diffraction, Fig. 3, as R-LCO (Type I) and s-LCO (Type II). These two regions have diffuse and wavy interfaces. Based on a number of observations in different parts of the film, we conclude that the Type II regions are structural minority domains embedded in r-LCO. Positions

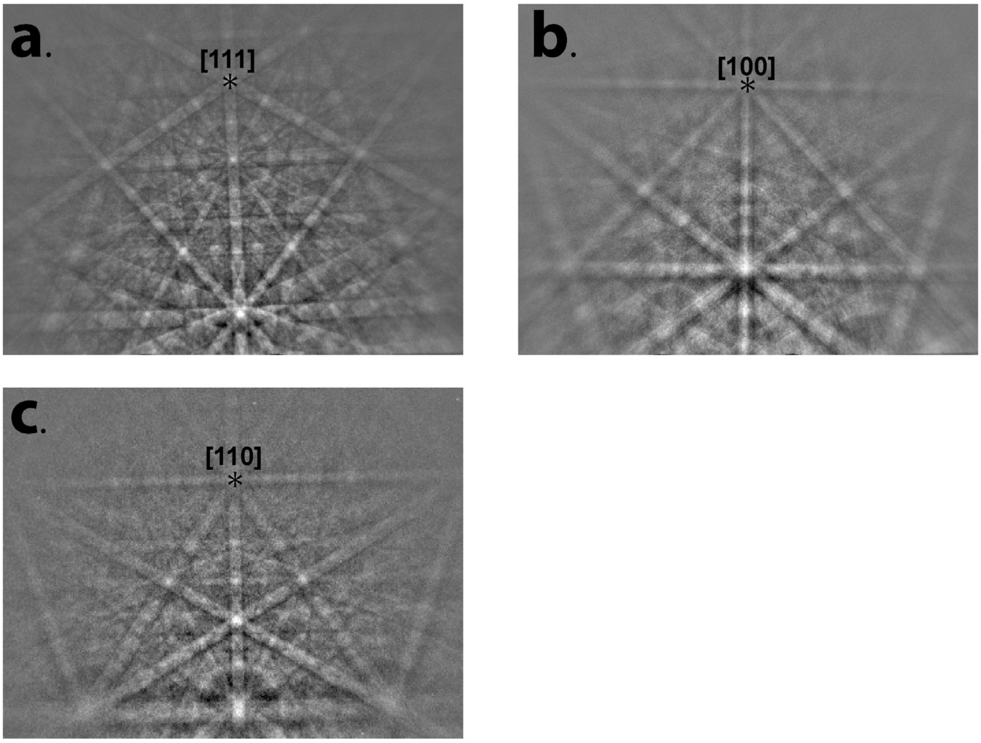

Fig. 7. Examples of EBSD patterns from LCO films obtained for three STO surfaces, (a) (111), (b) (100) and (c) (110). STO poles normal to the films' surfaces are indicated.

of the bright spots on the image corresponding to high-Z Co atomic columns were fitted with a few known LCO structures. The fitting clearly shows that the Type I structure is trigonal R-LCO, whereas the Type II structure fit spinel-like arrangement of either low temperature s-LCO or Li deficient $LiCo_2O_4$. Fig. 11b shows relative positions of Co and O atomic columns in the neighboring domains of R-LCO and s-LCO based on the experimental HAADF-STEM image; from this fitting it is clear that two structures have perfectly aligned continuous layers of Co octahedra.

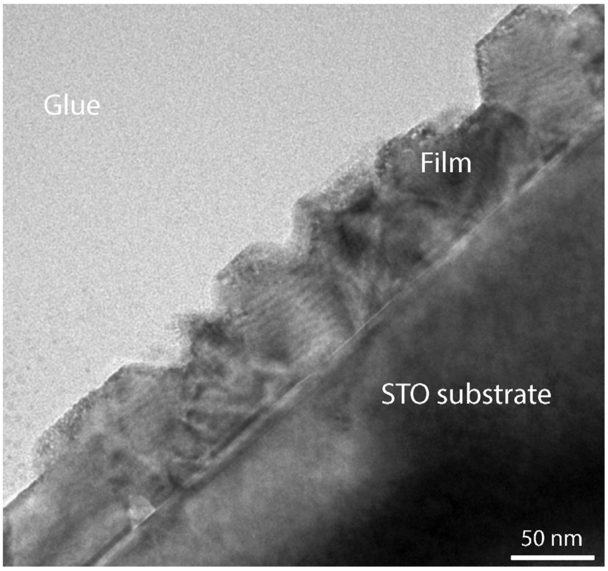

Fig. 8. Cross-sectional BF images of LCO(111) showing facetted nature of the film's surface.

3.4. Electrochemical measurements of the LCO films

Electrochemical measurements of the films using setup described in Experimental section did not resulted in observation of redox peaks (Fig. 12 for LCO/Nb:STO, blue line), as reported in literature for different LCO thin films, e.g., deposited by PLD on Pt [49] or stainless steel [50] substrates. In contrast, LCO deposited at the same condition on SROshowed typical behavior of LCO as reported in literature mentioned above (Fig. 12 for LCO on SRO/STO, black line). Furthermore, ICP measurements of the studied films demonstrated $Li_1Co_1O_2$ composition (accuracy of ±10%), which suggests, along with the microscopy results, that the absence of redox peaks is not due to the deficiency in lithium. The reason for not observing redox peaks can be explained by heterojunction at LCO/Nb-STO interface.

Schematic diagram of Fermi level (E_F) of LCO, and conduction band minimum (CBM) and valence band maximum (VBM) of Nb-STO is shown in Fig. 13a. The E_F of LCO is at −4.0 eV vs. Li/Li^+ [51]. Considering redox potential of lithium is −3.03 V vs. normal hydrogen electrode (N. H. E.) and hydrogen reference electrode is −4.48 eV vs. vacuum [52], E_F of LCO is calculated to be at −5.5 eV ($4.0–3.03 + 4.48 = 5.45 =$ ca. 5.5 eV) vs. vacuum. Work functions of SRO and Nb-STO (0.05 wt.%) is reported to be 5.2 and 4.1 eV from secondary electron emission spectra [53]. The difference between E_F of LCO and work function of SRO is 0.3 eV while the difference is 1.4 eV with Nb-STO (0.05 wt.%). Schottky barrier heights between SRO/Nb-STO 0.01 and 0.5 wt.% are reported to be 1.47 eV and 1.31 eV, respectively [54] which shows that the barrier height difference change is 0.16 eV smaller with doping of 0.5 wt.%. Hence it is expected that band offset of LCO/Nb-STO of 0.5 wt.% could be smaller than 1.4 eV, although not good enough to carry out well-controlled electrochemical measurement of LCO.

Direction of electron movement for both oxidation and reduction of LCO is illustrated in Fig. 13b. Oxidation of LCO, which should take place in sweeping voltage from OCV to 4.2 V, is reverse bias for LCO/Nb-STO heterojunction, which explains the absence of the clear oxidation peak

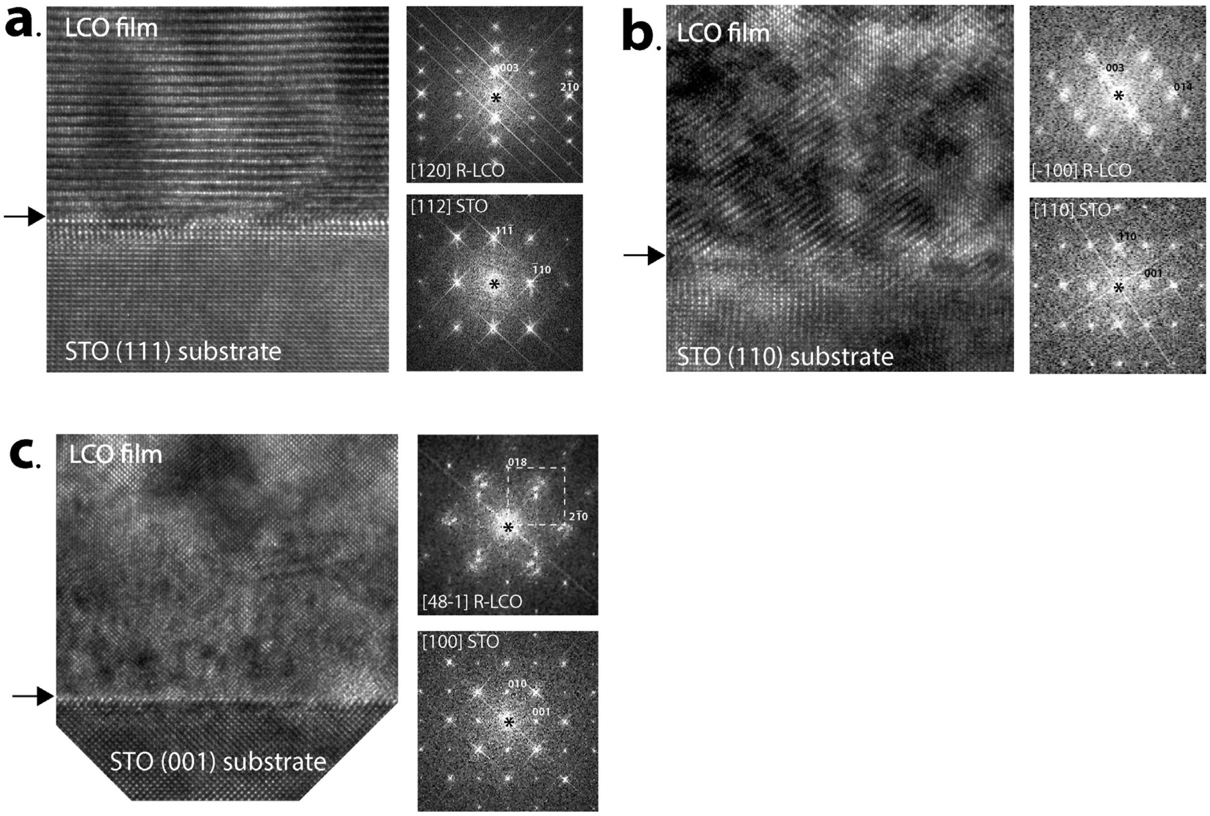

Fig. 9. (a) SAED pattern from the LCO(011) sample taken with a selected area aperture that includes both a film and a substrate in [100]STO zone axis orientation. (b) The substrate is in [100] zone axis (grey spots in diagram), and the LCO reflections are indexed as those of the [841] zone axis of R-LCO..

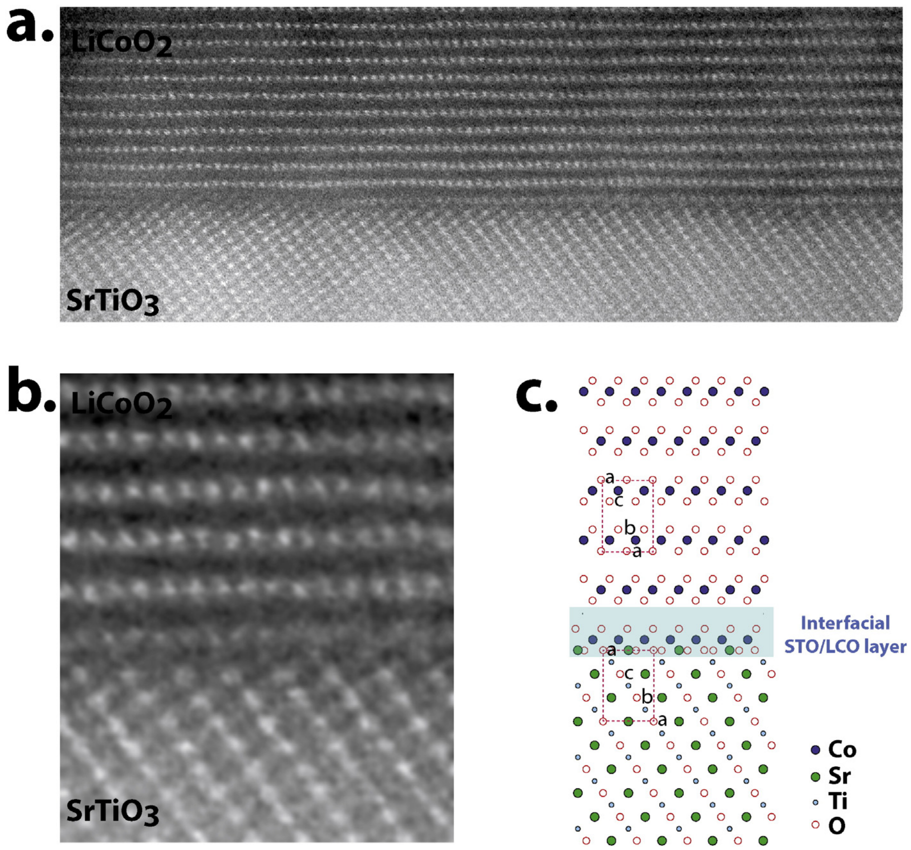

Fig. 10. (a) HAADF-STEM atomic imaging of the (111)STO/LCO interface. (b) Higher magnification showing positions of Sr,Ti and Co atomic columns. (c) Based on the image in (b) a structural model presents atomic positions at the interface.

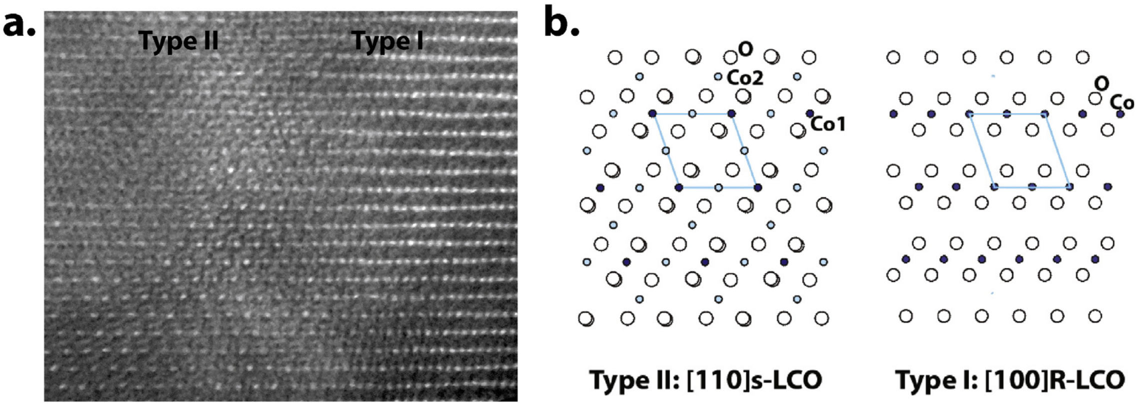

Fig. 11. (a) HAADF-STEM image of the (111)STO/LCO film in [211]STO orientation showing structural variations labeled as Type I and II. (b) Analysis of the bright spots' distribution gives two structures, trigonal R-LCO for Type I, and spinel-like LT-LCO for Type II. The projected structures.

from LCO. On the other hand, reduction of LCO, which takes place sweeping from 4.2 V to OCV, is forward bias and LCO/Nb-STO junction would not restrict the reaction.

Since the 1.4 eV band offset causes rectification at interface between LCO and Nb-STO, LCO/Nb-STO system is not ideal for studying electrochemical behavior of $LiCoO_2$ thin film. One way to deal with the problem is to have a buffer layer that has closer Fermi level to LCO, while structurally will not perturb the epitaxial film growth. Fermi level of perovskite-type $SrRuO_3$ (SRO) is reported to be 5.2 eV [53], which is 0.3 eV different from that of LCO. Furthermore, SRO epitaxial thin film deposited on STO shows high conductivity as $<2 \times 10^{-3}\ \Omega \cdot cm$ [55]; also epitaxial growth on SRO was shown for $LiMn_2O_4$. The possibility of studying electrochemical property of lithium transition metal oxide deposited on SRO was shown in [56]. Hence, as a continuation of this work, we studied electrochemical property of LCO thin films grown with a SRO buffer layer deposited on STO, and the results were reported elsewhere [57].

4. Summary

In this work we investigated possibilities of synthesizing $LiCoO_2$ single orientation films that could be used as a cathode for either all-solid state film-based Li-ion battery; such batteries could be utilized for detailed fundamental studies, including in situ electron microscopy, of electrochemical processes including structural transformations, anisotropy of Li diffusion, and interfacial reactions. PLD-grown $LiCoO_2$ epitaxial films on conductive Nb—$SrTiO_3$ single-crystal substrates of (111), (110) and (100) surface orientations were investigated in details by SEM, TEM and electrochemical testing.

In spite of the island growth mode, the films are assembled into a single orientation relationship with a substrate and can be called pseudo-epitaxial. For three orientations of STO substrates the formation of predominately trigonal R-$LiCoO_2$ phase was established, with a small fraction of the occasionally present cubic c-Li_xCoO_2 phase. Based on XRD and TEM diffraction, a single orientation relationship between R-$LiCoO_2$ and STO was established: $(111)_{STO}//(001)_{R\text{-}LTMO}$, $[110]_{STO}//[110]_{R\text{-}LTMO}$. However different 2-D symmetries of the substrate's surfaces dictate the presence of different orientational domains characterized by different direction of either c-axis or a-axis. The established orientation relationship can be considered as established by continuation of an oxygen sublattice from STO to LCO.

With the island growth mode the surface morphology of the films is established by the morphology of coalescing grains. Morphology of the grains is determined by orientation relationship and minimum energy surfaces and shape of the grains can be visualized as different cuts from a cube with $\{104\}_{R\text{-}LCO}$ surfaces. Accordingly, for the LCO(111) films the grains grow as truncated triangular pyramids, for LCO(100) films – cubes, and for LCO(110) films – truncated triangular prisms.

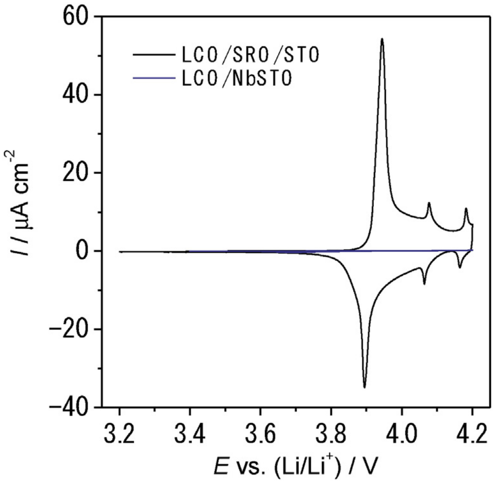

Fig. 12. Cyclic voltammogram of LCO in 1 mol dm^{-3} $LiClO_4$/PC from OCV – 4.2 V. Scan rate was 0.1 mV sec^{-1}. Black: LCO has $SrRuO_3$ buffer layer as a current collector between STO substrate. Blue: LCO directly deposited on Nb-STO.

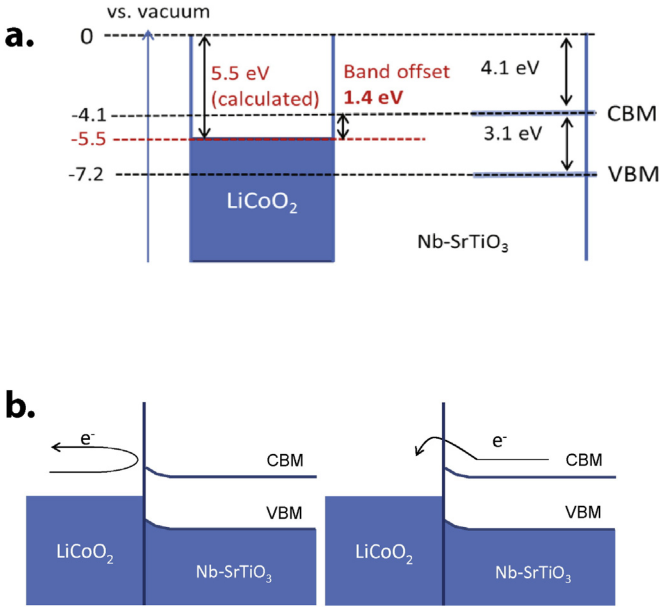

Fig. 13. (a) Schematic of band positions of $LiCoO_2$ and Nb-$SrTiO_3$ (b) Schematic of band diagram reverse bias (oxidation of $LiCoO_2$) and forward bias (reduction of $LiCoO_2$).

The observed facets are predominately non-polar low energy $\{104\}_{R\text{-}LCO}$, which determines non-flat surfaces of the films.

The Nb-doped single-crystal STO has sufficient conductivity to act not only as an orientation-inducing substrate but also as an electrode. However during electrochemical experiments it was determined that rectification at interface between LCO and Nb-STO causes bias on oxidation, thus preventing full cycling. This problem was successfully resolved in our follow-up work by coating STO with $SrRuO_3$ film, which preserved epitaxial growth of the LCO films and at the same time acted as reasonably good electrode allowing full cycling.

References

[1] N.J. Dudney, Solid-state thin-film rechargeable batteries, J. Mater. Sci. Eng. B 116 (2005) 245–249.

[2] A. Patil, V. Patil, D.W. Shin, J.-W. Choi, D.-S. Paik, S.-J. Yoon, Issue and challenges facing rechargeable thin film lithium batteries—a review, Mater. Res. Bull. 43 (2008) 1913–1942.

[3] L. Baggetto, H.C.M. Knoops, R.A.H. Niessen, W.M.M. Kessels, P.H.L. Notten, 3D negative electrode stacks for integrated all-solid-state lithium-ion microbatteries, J. Mater. Chem. 20 (2010) 3703.

[4] J. Besenhard (Ed.), Handbook of Battery Materials, Wiley-VCH, Weinheirn, New York, Chichester, Brisbane, Singapore, Toronto, 1999.

[5] R.A. Huggins, Advanced Batteries: Materials Science Aspects, Springer-Verlag, US, 2009.

[6] K.E. Aifantis, S.A. Hackney, R.V. Kumar (Eds.), High Energy Density Lithium Batteries, WILEY-VCH Verlag GmbH & Co. KGaA, Weinheim, 2010.

[7] K.H. Hwang, S.H. Lee, S.K. Joo, Characterization of sputter-deposited $LiMn_2O_4$ thin films for rechargeable microbatteries, J. Electrochem. Soc. 141 (1994) 3296–3299.

[8] J.F. Whitacre, W.C. West, B.V. Ratnakumar, The influence of target history and deposition geometry on RF magnetron sputtered $LiCoO_2$ thin films, J. Power Sources 103 (2001) 134–139.

[9] H. Pan, Y. Yang, Effects of radio-frequency sputtering powers on the microstructures and electrochemical properties of $LiCoO_2$ thin film electrodes, J. Power Sources 189 (2009) 633–637.

[10] J. Noh, G. Cho, K. Jung, W. Kang, C. Ha, H. Ahn, J. Ahn, T. Nam, K. Kim, Fabrication of $LiCoO_2$ thin film cathodes by DC magnetron sputtering method, Mater. Res. Bull. 47 (2012) 2823–2826.

[11] M.E. Donders, W.M. Arnoldbik, H.C. Knoops, W.M.M. Kessels, P.H.L. Notten, Atomic layer deposition of licoo2 thin-film electrodes for all-solid-state Li-Ion microbatteries, J. Electrochem. Soc. 160 (2013) A3066–A3071.

[12] M. Antaya, J.N. Reimers, W. Li, J.R. Dahn, Preparation and characterization of $LiCoO_2$ thin films by laser ablation deposition, J. Electrochem. Soc. 140 (1993) 575–578.

[13] K.A. Striebel, C.Z. Deng, S.J. Wen, E.J. Cairns, Electrochemical behavior of $LiMn_2O_4$ and $LiCoO_2$ thin films produced with pulsed laser deposition, J. Electrochem. Soc. 143 (1996) 1821–1827.

[14] J.D. Perkins, C.S. Bahn, P.A. Parilla, J.M. McGraw, M.L. Fu, M. Duncan, H. Yu, D.S. Ginley, $LiCoO_2$ and $LiCo_{1-x}Al_xO_2$ thin film cathodes grown by pulsed laser ablation, J. Power Sources 81–82 (1999) 675–679.

[15] Y. Iriyama, M. Inaba, T. Abe, Z. Ogumi, Preparation of *c*-axis oriented thin films of $LiCoO_2$ by pulsed laser deposition and their electrochemical properties, J. Power Sources 94 (2001) 175–182.

[16] S.B. Tang, L. Lu, M.O. Lai, Characterization of a $LiCoO_2$ thin film cathode grown by pulsed laser deposition, Philos. Mag. 85 (2005) 2831–2842.

[17] M. Hirayama, N. Sonoyama, T. Abe, M. Minoura, M. Ito, D. Mori, A. Yamada, R. Kanno, T. Terashima, M. Takano, K. Tamura, J. Mizuki, Characterization of electrode/electrolyte interface for lithium batteries using in situ synchrotron X-ray reflectometry—A new experimental technique for $LiCoO_2$ model electrode, J. Power Sources 168 (2007) 493–500.

[18] T. Ohnishi, K. Takada, High-rate growth of high-crystallinity $LiCoO_2$ epitaxial thin films by pulsed laser deposition, Appl. Phys. Express 5 (2012) 055502.

[19] K. Sakamoto, T. Hiraide, D. Mori, A. Yamada, R. Kanno, Characterization of electrode/electrolyte interface using in situ X-ray reflectometry and $LiNi_{0.8}Co_{0.2}O_2$ epitaxial film electrode synthesized by pulsed laser deposition method, Electrochim. Acta 53 (2007) 871–881.

[20] K. Nishio, T. Ohnishi, K. Akatsuka, K. Takada, Crystal orientation of epitaxial $LiCoO_2$ films grown on $SrTiO_3$ substrates, J. Power Sources 247 (2014) 687–691.

[21] C.H. Chen, A.A.J. Buysman, E.M. Kelder, J. Schoonman, Fabrication of $LiCoO_2$ thin film cathodes for rechargeable lithium battery by electrostatic spray pyrolysis, Solid State Ionics 80 (1995) 1–4.

[22] H.S.W. Chang, T.J. Lee, S.C. Lin, J.H. Jeng, 2/3 A-size rechargeable battery employing LiCoO2 thin-film cathode, J. Power Sources 54 (1995) 403–405.

[23] Y.H. Rho, K. Kanamura, T. Umegaki, $LiCoO_2$ and $LiMn_2O_4$ thin-film electrodes for rechargeable lithium batteries: Preparation using PVP Sol-gel to produce excellent electrochemical properties, J. Electrochem. Soc. 150 (2003) A107–A111.

[24] M. Kim, K. Park, D. Kim, J. Son, H. Kim, Effects of drying temperature on the $LiCoO_2$ Thin films fabricated by Sol-gel method, J. Korean Ceram. Soc. 38 (2001) 777–781.

[25] P. Fragnaud, R. Nagarajan, D.M. Schleich, D. Vujic, Thin-film cathodes for secondary lithium batteries, J. Power Sources 54 (1995) 362–366.

[26] E. Rossen, J.N. Reimers, J.R. Dahn, Synthesis and electrochemistry of spinel LT-$LiCoO_2$, Solid State Ionics 62 (1993) 53–60.

[27] R.J. Gummow, D.C. Liles, M.M. Thackeray, W.I.F. David, A reinvestigation of the structures of lithium-cobalt-oxides with neutron-diffraction data, Mater. Res. Bull. 28 (1993) 1177–1184.

[28] T. Abe, T. Koyama, Thermodynamic modeling of the $LiCoO_2$–CoO_2 pseudo-binary system, Calphad 35 (2011) 209–218.

[29] K. Chang, B. Hallstedt, D. Music, Thermodynamic and electrochemical properties of the Li–Co–O and Li–Ni–O systems, Chem. Mater. 24 (2012) 97–105.

[30] H.J. Orman, P.J. Wiseman, Cobalt (III) lithium oxide, $CoLiO_2$: structure refinement by powder neutron diffraction, Acta Crystallogr. C C40 (1984) 12–14.

[31] R.J. Gummow, D.C. Liles, M.M. Thackeray, Spinel versus layered structures for lithium cobalt oxide synthesised at 400 °C, Mater. Res. Bull. 28 (1993) 235–246.

[32] E. Rossen, J.N. Reimers, J.R. Dahn, Synthesis and electrochemistry of spinel LT-$LiCoO_2$, Solid State Ionics 62 (1993) 53–60.

[33] R.J. Gummow, D.C. Liles, M.M. Thackeray, W.I.F. David, A reinvestigation of the structures of lithium-cobalt- oxides with neutron-diffraction data, Mater. Res. Bull. 28 (1993) 1177–1184.

[34] M. Antaya, K. Cearns, J.S. Preston, J.N. Reimers, J.R. Dahn, In situ growth of layered, spinel, and rock-salt $LiCoO_2$ by laser ablation deposition, J. Appl. Phys. 76 (1994) 2799.

[35] H. Porthault, R. Baddour-Hadjean, F. Le Cras, C. Bourbon, S. Franger, Raman study of the spinel-to-layered phase transformation in sol–gel $LiCoO_2$ cathode powders as a function of the post-annealing temperature, Vib. Spectrosc. 62 (2012) 152–158.

[36] J.N. Reimers, J.R. Dahn, Electrochemical and in situ X-ray diffraction studies of lithium intercalation in Li_xCoO_2, J. Electrochem. Soc. 139 (1992) 2091–2097.

[37] M. Catti, Ab initio study of Li^+ diffusion paths in the monoclinic $Li_{0.5}CoO_2$ intercalate, Phys. Rev. B 61 (2000) 1795–1803.

[38] K. Mukai, H. Nozaki, Y. Ikedo, J. Sugiyama, K. Ariyoshi, T. Ohzuku, X-ray diffraction study on Li_xCoO_2 below ambient temperature, J. Power Sources 192 (2009) 684–688.

[39] Y. Shao-Horn, S. Levasseur, F. Weill, C. Delmas, Probing lithium and vacancy ordering in O_3 layered Li_xCoO_2 (x approximate to 0.5) - an electron diffraction study, J. Electrochem. Soc. 150 (2003) A366–A373.

[40] C. Wolverton, A. Zunger, First-principles prediction of vacancy order-disorder and intercalation battery voltages in Li_xCoO_2, Phys. Rev. Lett. 81 (1998) 606–609.

[41] A. Van der Ven, M. Aydinol, G. Ceder, G. Kresse, First-principles investigation of phase stability in $LixCoO_2$, Phys. Rev. B 58 (1998) 2975–2987.

[42] P.J. Bouwman, B.A. Boukamp, H.J.M. Bouwmeester, H.J. Wondergem, P.H.L. Notten, Structural analysis of submicrometer $LiCoO_2$ films, J. Electrochem. Soc. 148 (2001) A311–A317.

[43] H. Xia, L. Lu, Y.S. Meng, G. Ceder, Phase transitions and high-voltage electrochemical behavior of $LiCoO_2$ thin films grown by pulsed laser deposition, J. Electrochem. Soc. 154 (2007) A337–A342.

[44] S.B. Tang, L. Lu, M.O. Lai, Thin film microbatteries prepared by pulsed laser deposition, J. Korean Phys. Soc. 51 (2007) 1055–1062.

[45] Certain commercial equipment, instruments, or materials are identified in this document. Such identification does not imply recommendation or endorsement by the National Institute of Standards and Technology, nor does it imply that the products identified are necessarily the best available for the purpose.

[46] K. Sakamoto, H. Konishi, N. Sonoyama, A. Yamada, K. Tamura, J. Mizuki, R. Kanno, Mechanistic study on lithium intercalation using a restricted reaction field in $LiNi_{0.5}Mn_{0.5}O_2$, J. Power Sources 174 (2007) 678–682.

[47] P.W. Tasker, The stability of ionic crystal surfaces, J. Phys. C Solid State Phys. 12 (1979) 4977–4984.

[48] D. Kramer, G. Ceder, Tailoring the morphology of $LiCoO_2$: a first principles study, Chem. Mater. 21 (2009) 3799–3809.

[49] I. Yamada, Y. Iriyama, T. Abe, Z. Ogumi, Lithium-ion transfer on a Li_xCoO_2 thin film electrode prepared by pulsed laser deposition—effect of orientation-, J. Power Sources 172 (2007) 933–937.

[50] S.B. Tang, L. Lu, M.O. Lai, Characterization of a $LiCoO_2$ thin film cathode grown by pulsed laser deposition, Philos. Mag. 85 (2005) 2831–2842.

[51] J.B. Goodenough, Y. Kim, Challenges for rechargeable Li batteries, Chem. Mater. 22 (2010) 587–603.

[52] S. Roy Morrison, Electrochemistry at Semiconductor and Oxidized Metal Electrodes, Plenum Press New York, 1980.

[53] K. Morito, T. Suzuki, S. Sekiguchi, H. Okushi, M. Fujimoto, Electrical characterization of $SrTiO_3$ thin films grown on Nb-doped $SrTiO_3$ single crystals, Jpn. J. Appl. Phys. 39 (2000) 166–171.

[54] X. Fang, T. Kobayashi, Study of pulsed laser deposition of RuO_2 and $SrRuO_3$ thin films, Appl. Phys. A Mater. Sci. Process. 69 (1999) S587–S590.

[55] T. Ohnishi, K. Takada, Epitaxial thin-film growth of $SrRuO_3$, $Sr_3Ru_2O_7$, and Sr_2RuO_4 from a $SrRuO_3$ target by pulsed laser deposition, Appl. Phys. Express 4 (2011) 025501.

[56] K. Suzuki, K. Kim, S. Taminato, M. Hirayama, R. Kanno, Fabrication and electrochemical properties of $LiMn_2O_4$/$SrRuO_3$ multi-layer epitaxial thin film electrodes, J. Power Sources 226 (2013) 340–345.

[57] S. Takeuchi, H. Tan, K.K. Bharathi, G.R. Stafford, J. Shin, S. Yasui, I. Takeuchi, L.A. Bendersky, Epitaxial $LiCoO_2$ films as a model system for fundamental electrochemical studies of positive electrodes, ACS Appl. Mater. Interfaces 7 (2015) 7901–7911.